Propulsion driven by self-oscillation via an electrohydrodynamic instability

Lailai Zhu and Howard A. Stone

Propulsion driven by self-oscillation via an electrohydrodynamic instability

Lailai Zhu[1, 2] and Howard A. Stone[1, *]

[1]*Department of Mechanical and Aerospace Engineering,*
Princeton University, Princeton, NJ 08544, USA
[2]*Linné Flow Centre and Swedish e-Science Research Centre (SeRC), KTH Mechanics, Stockholm, SE-10044, Sweden*

Oscillations of flagella and cilia play an important role in biology, which motivates the idea of functional mimicry as part of bio-inspired applications. Nevertheless, it still remains challenging to drive their artificial counterparts to oscillate via a steady, homogeneous stimulus. Combining theory and simulations, we demonstrate a strategy to achieve this goal by using an elasto-electro-hydrodynamic instability. In particular, we show that applying a uniform DC electric field can produce self-oscillatory motion of a microrobot composed of a dielectric particle and an elastic filament. Upon tuning the electric field and filament elasticity, the microrobot exhibits three distinct behaviors: a stationary state, undulatory swimming and steady spinning, where the swimming behavior stems from an instability emerging through a Hopf bifurcation. Our results imply the feasibility of engineering self-oscillations by leveraging the elasto-viscous response to control the type of bifurcation and the form of instability. We anticipate that our strategy will be useful in a broad range of applications imitating self-oscillatory natural phenomena and biological processes.

Flagella and cilia exhibit oscillatory movements for locomotion, pumping and fluid mixing. To mimic these functionalities, various approaches have been developed to oscillate their artificial counterparts using magnetic [1, 2], electrostatic [3], piezoelectric [4], optical [5] and hydrogel-based actuations [6, 7]. In general, a time-dependent stimulus generates oscillations in many biomimetic systems. An apparent exception is the use of the Belousov-Zhabotinsky (BZ) oscillating chemical reaction [7] (inspired by Ref [8]) to deform polymer brushes periodically. Nonetheless, time-dependent forcing is not necessary for biological systems which can occasionally generate oscillations by steady stimuli to deliver functionalities such as otoacoustic emissions [9, 10] and glycolysis [11], etc. These behaviors, namely, the generation and maintenance of a periodic motion powered by a source without a corresponding periodicity is referred to as self-oscillation [12, 13].

Self-oscillation plays a crucial role in some inertia-dominated flow cases, such as the collapse of the Tacoma Narrows Bridge [14] and the sound generation of wind musical instruments (including whistling and the human voice), owing to inertia-induced nonlinearity. In this Rapid Communication, we create self-oscillations of artificial structures in a situation with negligible inertia by applying a uniform, time-independent electric field. We exploit an elasto-electro-hydrodynamic (EEH) instability by marrying an electrohydrodynamic instability with an elasto-viscous response. Combining theory and simulations, we investigate a composite microrobot that achieves unidirectional locomotion by self-oscillatory wiggling of an elastic appendage.

It was discovered in 1896 by Quincke [15] that a uniform DC electric field can trigger the spontaneous rotation of a dielectric particle immersed in a dielectric solvent with higher conductivity. Quincke rotation (QR) occurs as an electrohydrodynamic instability emerging from an equilibrium configuration where the induced-charge dipole $\mathcal{P}$ of the particle is opposite to the applied field. When the field strength E exceeds a threshold value, E^{cri}, the symmetric yet antiparallel configuration is unstable to an infinitesimal disturbance, spontaneously breaking the mirror symmetry through a supercritical pitchfork bifurcation [16, 17]; the particle then spins steadily where the electric and viscous torques balance.

We exploit this QR instability by grafting an inextensible elastic filament of radius a and length L onto a dielectric spherical particle of radius A (Fig. 1a), where s denotes the arclength of the filament's centerline with position $\mathbf{r}(s, t)$, and $\alpha = A/L$ is the size ratio. The slenderness of the filament $\epsilon_{\mathrm{sl}} = a/L \ll 1$. The filament base $s = 0$ is clamped at the particle surface J, where the tangent vector $\mathbf{e}_{\mathrm{p}} = \partial \mathbf{r}/\partial s|_{s=0}$ at the base always passes through the particle center P and $\mathbf{e}_{\mathrm{p}}$ denotes the orientation of the object. We define an elasto-electro-viscous (EEV) parameter $\bar{\mu} = 8\pi\mu L^4/D\tau_{\mathrm{s}}$ indicating the ratio of the elasto-viscous time scale $8\pi\mu L^4/D$ to the charge relaxation time $\tau_{\mathrm{s}} = \epsilon_{\mathrm{s}}/\sigma_{\mathrm{s}}$ of the solvent, where μ, ϵ_{s} and σ_{s} denote respectively, the dynamic viscosity, permittivity and conductivity of the solvent, and D is the bending stiffness of the filament. $\bar{\mu}$ indicates the relative strength of the viscous to the elastic forces, where $\bar{\mu} = 0$ corresponds to a rigid filament and increasing $\bar{\mu}$ corresponds to a more compliant filament. To focus on the elasto-viscous response of the filament, we do not consider its polarization. We also do not take into account the hydrodynamic interactions between the particle and the filament.

We adopt the proper Euler angles $[\theta, \phi, \psi]$ to characterize the rotation of the object. The uniform electric field $\mathbf{E} = E\mathbf{e}_z$ and the particle dipole $\mathcal{P}$ are expressed in the reference coordinate system $[\mathbf{N}, \mathbf{Q}, \mathbf{e}_3]$ rotating and translating with the object, where $\mathbf{e}_3$ coincides with the its orientation $\mathbf{e}_{\mathrm{p}}$, $\mathbf{N}$ indicates the nodal line direction and $\mathbf{Q} = \mathbf{e}_3 \times \mathbf{N}$
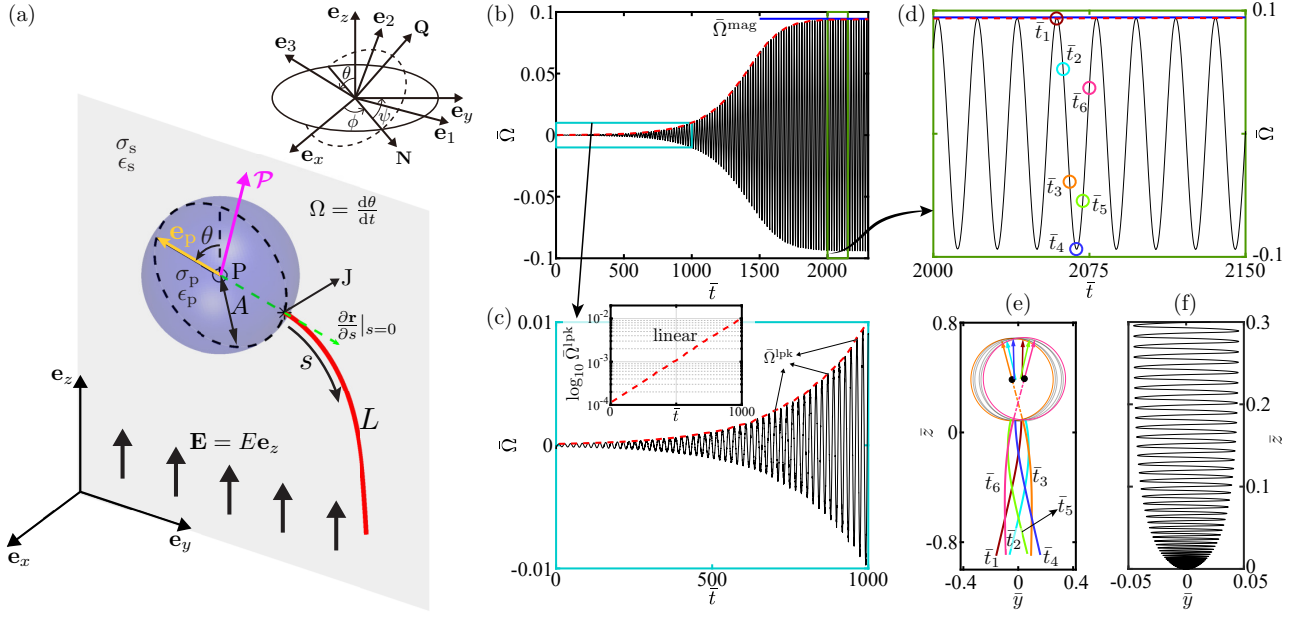
FIG. 1: Self-oscillation of a composite particle and filament. (a) A dielectric sphere of radius A, with an attached filament of radius a, contour length L, size ratio $\alpha = A/L = 0.3$ and elasticity characterized by the EEV number $\bar{\mu} = 635$, is under a steady uniform electrical field $\mathbf{E} = E\mathbf{e}_z$; the particle dipole is $\mathcal{P}$. The upright panel depicts the Euler angles $[\theta, \phi, \psi]$ describing the rotation of the object and the reference coordinate system $[\mathbf{e}_N, \mathbf{e}_Q, \mathbf{e}_3]$, where $\mathbf{e}_3$ is aligned with the object's orientation $\mathbf{e}_p$. The object's motion is constrained to the yz-plane, and its orientation $\mathbf{e}_p \equiv \mathbf{e}_3$ is directed at an angle θ with respect to $\mathbf{e}_z$. (b) The composite object's dimensionless rotational velocity $\bar{\Omega} = d\theta/d\bar{t}$ oscillates over dimensionless time $\bar{t}$ with a local peak value $\bar{\Omega}^{\text{lpk}}$. The time evolution of $\bar{\Omega}$ is characterized by two periods, as $\bar{\Omega}^{\text{lpk}}$ increases exponentially in the initial phase (cyan box) and eventually reaches a constant magnitude $\bar{\Omega}^{\text{mag}}$ (green box). (c) Exponential growth of $\bar{\Omega}$ in the initial phase $\bar{t} \in [0, 1000]$ is indicated by the inset showing the linear dependence of $\log \bar{\Omega}^{\text{lpk}}$ on $\bar{t}$. (d) Periodic variation of $\bar{\Omega}$ with a constant amplitude; six times $\bar{t}_i, i = 1, .., 6$ within one period are marked. (e) Orientation of the composite object and the filament shape at $\bar{t}_i$. (f) Trajectory of the particle center P in the yz-plane during the period $\bar{t} \in [0, 1940]$.

(Fig. 1a). We constrain the object's motion to the yz-plane, hence the dipole $\mathcal{P}$, the orientation $\mathbf{e}_p$, and the filament lie in the same plane, resulting in $\mathbf{N} = \mathbf{e}_x$. Using $\tau_s, \tau_s^{-1}, D/L, E^{\text{cri}}$ and $D/(LE^{\text{cri}})$ as the characteristic time, rotation rate, torque, electrical field and polarization dipole strength, respectively, the nondimensional electrohydrodynamic equations are [18] [19]

$$\partial\theta/\partial\bar{t} = \left(\bar{\Gamma}_N^{\text{f}\to\text{p}} + \bar{E}_3\bar{\mathcal{P}}_Q - \bar{E}_Q\bar{\mathcal{P}}_3\right)/\bar{\eta}, \tag{1a}$$

$$\partial\bar{\mathcal{P}}_Q/\partial\bar{t} = -\kappa\left(\bar{\mathcal{P}}_Q + \kappa\bar{\eta}\bar{E}_Q\right), \tag{1b}$$

$$\partial\bar{\mathcal{P}}_3/\partial\bar{t} = -\kappa\left(\bar{\mathcal{P}}_3 + \kappa\bar{\eta}\bar{E}_3\right), \tag{1c}$$

where $^-$ denotes dimensionless quantities hereafter, $\bar{\mathbf{\Gamma}}^{\text{f}\to\text{p}}$ is the elastic torque exerted by the filament onto the particle with respect to its center; $\bar{\eta} = \alpha^3\bar{\mu}$, $\kappa = (R+2)/(S+2)$, $R = \sigma_p/\sigma_s$ and $S = \epsilon_p/\epsilon_s$, where ϵ_p and σ_p are the permittivity and conductivity of the particle, respectively.

Applying a fixed electric field, $\bar{E} = 1.5$ for example, we discovered a self-oscillatory response of the composite object by tuning the filament elasticity (Fig. 1). When $\bar{\mu} = 635$, the particle wobbles spontaneously rather than to rotate steadily like the classical QR counterpart, as indicated by the rotational velocity $\bar{\Omega} = d\theta/d\bar{t}$ (Fig. 1b). The local peak $\bar{\Omega}^{\text{lpk}}$ of $\bar{\Omega}$ increases with $\bar{t}$ rapidly during the initial period and eventually saturates to a constant value $\bar{\Omega}^{\text{mag}}$ corresponding to a time-periodic state.

To understand the initial dynamics, we examine the initial phase $\bar{\Omega}(\bar{t})$, as shown in Fig. 1b (highlighted in the cyan box). This local peak $\bar{\Omega}^{\text{lpk}}$ (Fig. 1c) initially grows exponentially, as confirmed by the inset displaying the linear dependence of $\log \bar{\Omega}^{\text{lpk}}$ on $\bar{t}$. Thus, the self-oscillation arises through a linear instability mechanism, similar to other self-oscillation phenomena [12]. Furthermore, the system reaches a time-periodic state, namely, the particle oscillates with a fixed amplitude (Fig. 1d highlighting the green box of Fig. 1b). To understand how the grafted filament reacts to the particle, we show in Fig. 1e the particle-filament configurations at six times within a period. We observe that the
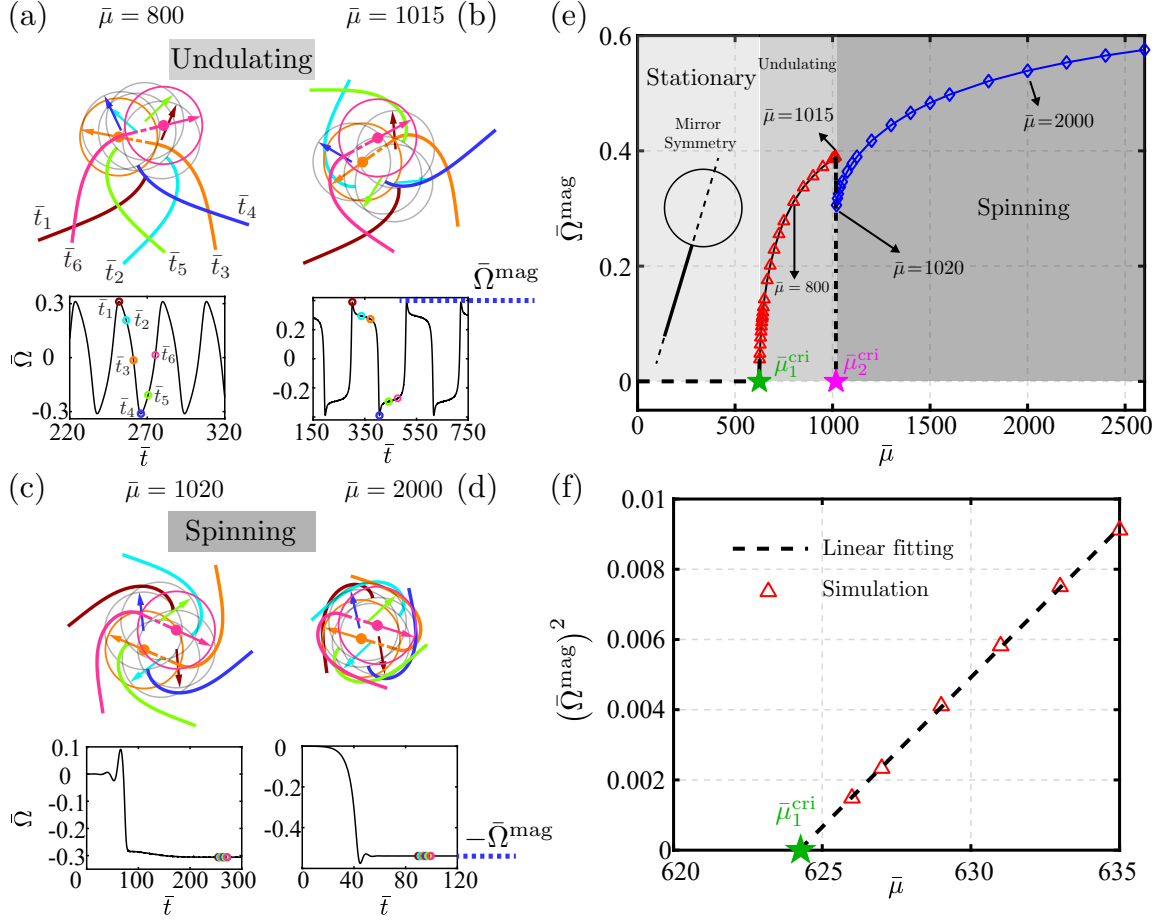
FIG. 2: Tuning the filament elasticity for various behaviors: stationary, undulating and spinning (see supplemental videos). (a) and (b) Results for $\bar{\mu} = 800$ and 1015: time evolution of $\bar{\Omega}$ when the object undulates periodically with a magnitude $\bar{\Omega}^{\mathrm{mag}}$, and the particle-filament configuration at six times within a period. The $\bar{\mu} = 1015$ case exhibits a large amplitude in the rotational displacement. (c) and (d) Similar to (a) and (b), but for $\bar{\mu} = 1020$ and 2000, when the system evolves from $\bar{t} = 0$ to its steady spinning state; six times are chosen within one rotational period. (e) The magnitude of rotational velocity $\bar{\Omega}^{\mathrm{mag}}$ versus $\bar{\mu}$. The system is stationary when $\bar{\mu} < \bar{\mu}_1^{\mathrm{cri}} \approx 625$, undulates when $\bar{\mu}_1^{\mathrm{cri}} < \bar{\mu} < \bar{\mu}_2^{\mathrm{cri}} \approx 1017$ and spins steadily when $\bar{\mu} > \bar{\mu}_2^{\mathrm{cri}}$. Two undulatory cases ($\bar{\mu} = 800$ and 1015) and two steady spinning ones ($\bar{\mu} = 1020$ and 2000) are marked. (f) Linear relation between $(\bar{\Omega}^{\mathrm{mag}})^2$ and μ close to $\bar{\mu}_1^{\mathrm{cri}}$.

oscillating particle drives the filament to wiggle, a scenario resembling the locomotion of a flagellated microorganism that acquires thrust by propagating oscillatory bending waves from the head towards the tail. A striking yet natural consequence of this self-oscillation is that the object undulates and translates, hence demonstrates propulsion by harnessing thrust from the wiggling filament.

A series of simulations was performed to examine the influence of the filament elasticity. By varying $\bar{\mu}$, we identify three states of the composite object: an undulatory motion (Fig. 2a,b, where $\bar{\mu} = 800$, 1015 respectively) similar to the $\bar{\mu} = 635$ case reported in Fig. 1d,e, though here we observe a larger oscillation amplitude characterized by $\bar{\Omega}^{\mathrm{mag}}$; and a steady spinning motion (Fig. 2c,d, where $\bar{\mu} = 1020$, 2000 respectively), resembling a QR particle towing a passively bent filament that breaks the mirror symmetry about the filament centerline; a stationary state when $\bar{\mu}$ is below a critical value, where the object is stationary ($\bar{\Omega} = 0$) and possesses mirror symmetry. The three elasticity-dependent states are identified with a dashed line (stationary), triangles (undulatory) and diamonds (spinning) in Fig. 2e, which represent the bifurcation diagram of a one-parameter ($\bar{\mu}$) dynamical system: the stationary state is a symmetric fixed-point solution, which transits through a supercritical Hopf bifurcation [20] at $\bar{\mu}_1^{\mathrm{cri}} \approx 625$ to a limit-cycle solution corresponding to the undulating state. This periodic solution jumps, via a secondary bifurcation at $\bar{\mu}_2^{\mathrm{cri}} \approx 1017$, to another asymmetric fixed-point solution representing the spinning state. The Hopf bifurcation is confirmed by the quadratic variation of $\bar{\Omega}^{\mathrm{mag}}$ in $\bar{\mu}$ in the vicinity of $\bar{\mu}_1^{\mathrm{cri}}$ shown in Fig. 2b (linear dependence of $(\bar{\Omega}^{\mathrm{mag}})^2$ on $\bar{\mu}$). It is

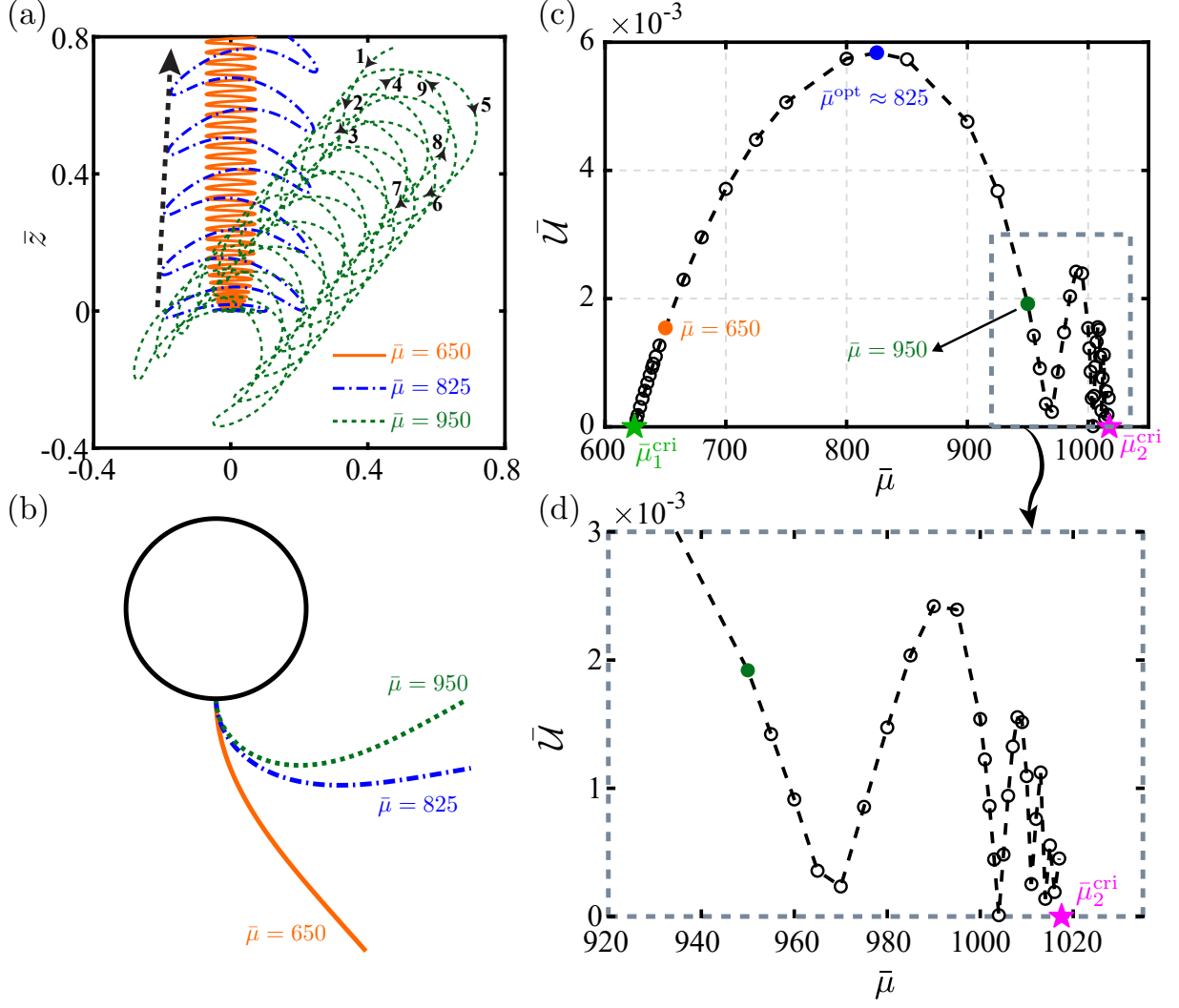FIG. 3: Self-oscillatory propulsion of the composite swimmer. (a) Planer swimming trajectories for $\bar{\mu} = 650$, 825 and 950. The dashed arrow indicates the on average straight trajectory of the $\bar{\mu} = 825$ swimmer. Arrows with numbers are marked at increasing times on the trajectory of $\bar{\mu} = 950$. (b) Maximum filament defection. (c) Effective translational velocity $\bar{\mathcal{U}}$ versus $\bar{\mu}$, reaching its peak at $\bar{\mu} = \bar{\mu}^{\mathrm{opt}} \approx 825$. (d) Close-up view of $\bar{\mathcal{U}}(\bar{\mu})$ in the regime where $\bar{\mathcal{U}}$ exhibits a wavelike variation near $\bar{\mu} \approx \bar{\mu}_2^{\mathrm{cri}}$.

worth-noting that the bifurcation diagram featured with these two bifurcations remains unchanged when the electric field $1 < \bar{E} < \bar{\mathcal{E}}^{\mathrm{cri}}$, where $\bar{\mathcal{E}}^{\mathrm{cri}}$ corresponds to the critical field above which the particle with a rigid filament ($\bar{\mu} = 0$) undergoes QR; when $\bar{E} > \bar{\mathcal{E}}^{\mathrm{cri}}$, the object spins steadily regardless of $\bar{\mu}$.

The composite object achieves self-oscillatory propulsion only in the undulating regime $\bar{\mu} \in \left(\bar{\mu}_1^{\mathrm{cri}}, \bar{\mu}_2^{\mathrm{cri}}\right)$, attaining zero net locomotion when $\bar{\mu} \to \bar{\mu}_1^{\mathrm{cri}}+$ and $\bar{\mu} \to \bar{\mu}_2^{\mathrm{cri}}-$. We expect its propulsive performance to exhibit a non-monotonic dependence on $\bar{\mu}$ and peaks at an optimal EEV parameter $\bar{\mu}^{\mathrm{opt}}$. We quantify the performance by the translational velocity $\bar{\mathcal{U}}$ of the swimmer along its effective straight path connecting the most convex points on the wavelike trajectory (Fig. 3a). The trajectory shape depends on $\bar{\mu}$: for the stiffest filament $\bar{\mu} = 650$, it matches a sinusoidal wave with a high frequency, almost preserving fore-aft temporal symmetry. Conversely, when $\bar{\mu} = 825$, the wavy trajectory is characterized by a larger amplitude and lower frequency. For the most floppy case shown $\bar{\mu} = 950$, the trajectory is significantly coiled, exhibiting a pronounced fore-aft asymmetry. Consequently, the swimmer's backward movement is comparable to the forward movement, leading to a nearly reciprocal motion. The increasing coiled trajectory for $\bar{\mu}$ is closely linked to the more deflected filament shown in Fig. 3b. Fig. 3c confirms our anticipation of the non-monotonically varying $\bar{\mathcal{U}}$ with peak value of $\bar{\mathcal{U}}^{\mathrm{opt}} \approx 6 \times 10^{-3}$ at $\bar{\mu}^{\mathrm{opt}} \approx 825$. This velocity $\bar{\mathcal{U}}^{\mathrm{opt}}$ lies in the range

$(1, 15) \times 10^{-3}$ of the dimensionless speed of a magnetically-driven flexible flagellum [21], implying the reasonable efficiency of this self-oscillatory propulsion mechanism. We notice that $\bar{\mathcal{U}}$ oscillates with $\bar{\mu}$ when $\bar{\mu} \to \bar{\mu}_2^{\mathrm{cri}}$. We do not attempt to unravel this peculiar variation here, keeping in mind that the main focus of the current work is on engineering self-oscillation to achieve various functionalities such as locomotion. A thorough analysis on the propulsive features of the microrobot will be conducted in future work.
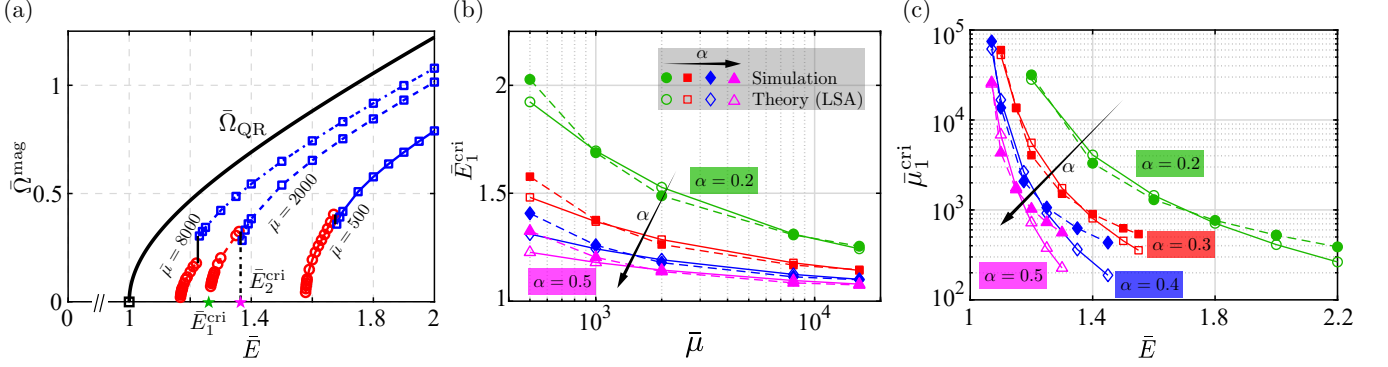

FIG. 4: (a) Bifurcation diagram considering $\bar{E}$ as the control parameter for different $\bar{\mu}$ values, where $\bar{E}_1^{\mathrm{cri}}$ and $\bar{E}_2^{\mathrm{cri}}$ indicate the emergence of the Hopf and the secondary bifurcations, respectively. $\bar{\Omega}_{\mathrm{QR}}$ denotes the original QR (no filament, $\bar{\mu} \to \infty$) velocity. (b) Critical electric field strength $\bar{E}_1^{\mathrm{cri}}$ versus $\bar{\mu}$, and (c) Critical EEV number $\bar{\mu}_1^{\mathrm{cri}}$ versus $\bar{E}$, for different size ratio α; filled and hollow symbols denote, respectively, the numerical and theoretical (LSA) predictions.

By varying $\bar{E}$, we present a bifurcation diagram in Fig. 4a for the composite object with different $\bar{\mu}$ values. The diagram shares the same feature with Fig. 2e considering $\bar{\mu}$ as the control parameter: a Hopf and a secondary bifurcation occur at $\bar{E}_1^{\mathrm{cri}}$ and $\bar{E}_2^{\mathrm{cri}}$, respectively. $\bar{E} = 1$ (hollow square) indicates the pitchfork bifurcation resulting in the original QR instability. This graph has highlighted the role of the filament in transforming the pitchfork bifurcation into the Hopf bifurcation that leads to self-oscillation. We further conduct a linear stability analysis (LSA) [22] around an equilibrium base solution $[\theta, \bar{\mathcal{P}}_Q, \bar{\mathcal{P}}_3] = [\hat{\theta}, -\kappa \bar{\eta} \bar{E} \sin \hat{\theta}, -\kappa \bar{\eta} \bar{E} \cos \hat{\theta}]$ of Equ. 1 ($\hat{\theta}$ can be an arbitrary value without loss of generality), when the composite system is stationary and the filament is undeformed. Without the filament, $\bar{\Gamma}_N^{\mathrm{f} \to \mathrm{p}} = 0$, the LSA indeed predicts a critical electrical field of $\bar{E} = 1$ corresponding to that of the original QR instability. In the presence of filament, realizing that the filament undergoes weak deformation near the onset of instability, we are able to model the elastic torque $\bar{\Gamma}_N^{\mathrm{f} \to \mathrm{p}}$ following Refs. [23, 24]. The critical electric field $\bar{E}_1^{\mathrm{cri}}$ predicted by LSA above which self-oscillatory instability occurs is shown as a function of $\bar{\mu}$ and α (Fig. 4b), so as the critical EEV number $\bar{\mu}_1^{\mathrm{cri}}$ versus $\bar{E}$ and α (Fig. 4c). These theoretical predictions agree well with their numerical counterparts, especially when $\bar{\mu}$ is large.

In this work, we have uncovered an EEH instability and demonstrated a strategy for engineering self-oscillations based on a steady, uniform electric field. This idea is illustrated by driving the motion of a dielectric particle connected to an elastic filament. By tuning the filament elasticity and electric field strength, the object achieves propulsion enabled by the dual functionalities of the filament: manipulating the bifurcation through its elasto-viscous response, which causes the particle to oscillate; providing thrust by wiggling motion actuated by the oscillating particle. Besides offering the possibility as a swimming microrobot, the object can also transform into a stationary, soft obstacle or spinner when the electric field strength is tuned, respectively, below or above the critical values we have identified.

The key idea we have recognized is to introduce an elastic element to trigger the Hopf bifurcation and consequently the self-oscillatory instability. Therefore, this might be one path for engineering biomimetic oscillatory processes using a time-independent power source. More generally, our results imply the potential for incorporating elastic media in other unstable systems to manipulate and diversify the bifurcations [25], which possibly can be employed for different functionalities. This concept is different from, but complementary to, taming a structure's mechanical failures to achieve functionalities [26]. We believe that our ideas offer opportunities to develop a new generation of soft, reconfigurable machines that can morph and adapt to the environment. Experiments to test and further explore the EEH instability introduced in this work are in progress.

was provided by SNIC (Swedish National Infrastructure for Computing).

––––––––––––

* Electronic address: hastone@princeton.edu

[1] H. Singh, P. E. Laibinis, and T. A. Hatton, Nano Lett. **5**, 2149 (2005).

[2] B. A. Evans, A. R. Shields, R. L. Carroll, S. Washburn, M. R. Falvo, and R. Superfine, Nano Lett. **7**, 1428 (2007).

[3] J. den Toonder, F. Bos, D. Broer, L. Filippini, M. Gillies, J. de Goede, T. Mol, M. Reijme, W. Talen, H. Wilderbeek, et al., Lab Chip **8**, 533 (2008).

[4] O. Kieseok, J.-H. Chung, S. Devasia, and J. J. Riley, Lab Chip **9**, 1561 (2009).

[5] C. L. van Oosten, C. W. M. Bastiaansen, and D. J. Broer, Nat. Mater. **8**, 677 (2009).

[6] A. Sidorenko, T. Krupenkin, A. Taylor, P. Fratzl, and J. Aizenberg, Science **315**, 487 (2007).

[7] T. Masuda, M. Hidaka, Y. Murase, A. M. Akimoto, K. Nagase, T. Okano, and R. Yoshida, Angew. Chem. **125**, 7616 (2013).

[8] R. Yoshida, T. Takahashi, T. Yamaguchi, and H. Ichijo, J. Am. Chem. Soc. **118**, 5134 (1996).

[9] T. Gold, Proc. R. Soc. London, Ser. B **135**, 492 (1948).

[10] D. T. Kemp, Arch. Otorhinolaryngol. **224**, 37 (1979).

[11] E. E. Sel'kov, Eur. J. Biochem. **4**, 79 (1968).

[12] A. Jenkins, Phys. Rep. **525**, 167 (2013).

[13] Self-oscillation is also known in other literature as "maintained", "sustained", "self-excited", "self-induced", "spontaneous" and "autonomous" oscillations [12].

[14] This phenomenon is mischaracterized by some introductory physics texts, where it is attributed to forced resonance.

[15] G. Quincke, Ann. Phys. **295**, 417 (1896).

[16] I. Turcu, J. Phys. A: Math. Gen. **20**, 3301 (1987).

[17] F. Peters, L. Lobry, and E. Lemaire, Chaos **15**, 013102 (2005).

[18] A. Cēbers, E. Lemaire, and L. Lobry, Phys. Rev. E **63**, 016301 (2000).

[19] See Supplemental Material at url for the detailed mathematical description of the EEH problem, which includes Refs. [18, 22, 27–31].

[20] S. H. Strogatz, Nonlinear Dynamics and Chaos: With Applications to Physics, Biology, Chemistry, and Engineering (1994).

[21] R. Dreyfus, J. Baudry, M. L. Roper, M. Fermigier, H. A. Stone, and J. Bibette, Nature **437**, 862 (2005).

[22] L. Zhu and H. A. Stone, To be submitted (2019).

[23] C. H. Wiggins and R. E. Goldstein, Phys. Rev. Lett. **80**, 3879 (1998).

[24] C. H. Wiggins, D. Riveline, A. Ott, and R. E. Goldstein, Biophys. J. **74**, 1043 (1998).

[25] G. Chen, J. L. Moiola, and H. O. Wang, Int. J. Bifurcation Chaos **10**, 511 (2000).

[26] P. M. Reis, F. Brau, and P. Damman, Nat. Phys. **14** (2018).

[27] Q. Brosseau, G. Hickey, and P. M. Vlahovska, Phys. Rev. Fluids **2**, 014101 (2017).

[28] G. K. Batchelor, J. Fluid Mech. **44**, 419 (1970).

[29] L. A. Segel, Mathematics Applied to Continuum Mechanics, vol. 52 (SIAM, 2007).

[30] A.-K. Tornberg and M. J. Shelley, J. Comput. Phys. **196**, 8 (2004).

[31] L. Li, H. Manikantan, D. Saintillan, and S. E. Spagnolie, J. Fluid Mech. **735**, 705 (2013).